Estimating stratospheric aerosols physical properties by Ruby-lidar observations

G. P. GOBBI (*)
Istituto di Fisica dell'Atmosfera, Consiglio Nazionale delle Ricerche
Via Fosso del Cavaliere 100, 00133 Roma, Italy

(ricevuto il 12 Settembre 1997; revisionato il 6 Aprile 1998; approvato il 27 Aprile 1998)

Summary. — An optical model originally developed at 532 nm is applied to the Ruby laser wavelength of 694 nm. Functional relationships resulting from the model allow estimates of stratospheric aerosol surface area, volume, extinction-to-backscatter ratio, extinction, and effective radius from single wavelength, Ruby-lidar measurements. These parametrizations are valid for global stratospheric sulphate aerosols and liquid polar stratospheric clouds. Relative errors of the estimates are in the range of 15–45% for surface area, 15–30% for volume, 20–35% for extinction-to-backscatter ratio and extinction, and 40–55% for effective radius. These errors are comparable to the ones characterizing direct, *in situ* techniques as optical particle counters. Comparisons with results of the original model at 532 nm are presented.

PACS 94.10.Gb – Absorption and scattering of radiation.
PACS 92.60.Mt – Particles and aerosols.
PACS 42.68 – Atmospheric Optics.

1. – Introduction

Stratospheric aerosols participate in the control of factors, such as global warming and cooling, chemistry of the ozone layer and atmospheric dynamics [1-3]. Their action maximizes after major volcanic eruptions and lasts for several years thanks to long decay times [1]. Conversely, the very low temperatures reached in the winter polar regions lead to the growth of background sulphate aerosols by condensation of ambient nitric acid and water [2]. The resulting optically thin clouds, known as polar stratospheric clouds (PSC), represent a seasonal, colder equivalent of volcanic aerosols. Thanks to their large surface area and settling speeds, PSC set up the conditions for the springtime "ozone hole" phenomenon, by both activating ozone-destroying halogens and sedimenting halogen-capturing nitrates [2]. In a similar fashion, volcanic

(*) E-mail: gobbi@sunifa1.ifsi.rm.cnr.it

aerosols enhance both ozone photodissociation and heterogeneous activation of ozone-depleting species, two processes resulting into a global, long-lasting ozone reduction [3].

The background stratospheric aerosol layer peaks at approximately 70 hPa and is formed by diluted sulphuric-acid droplets which remain supercooled, therefore spherical, down to at least 192 K [4-6]. In typical mid-latitude conditions, stratospheric aerosols are composed of 70–75% H_2SO_4 by weight, while in the colder high-latitude stratosphere they deliquesce to approximately 50% H_2SO_4-50% H_2O [7-9]. Below approximately 192 K, *i.e.* in polar winter conditions, ambient nitric acid condenses onto sulphate aerosols to form supercooled ternary solution (STS) PSC, which can remain liquid down to the ice frost point temperature [10]. The assumption of sphericity holds then for all these aerosols, whose scattering properties can be computed by means of the Mie theory.

This paper presents results obtained at the Ruby laser wavelength of 694 nm, by a model originally developed to estimate aerosols physical properties from Nd-YAG lidar returns at 532 nm [11]. Interest for the Ruby laser wavelength is justified by the large number of such lidars still in operation. On the basis of that model, functional relationships linking single-wavelength lidar backscatter at 694 nm to aerosols surface area, volume, extinction-to-backscatter ratio, extinction, and effective radius will be obtained. These results will be compared to the ones obtained at 532 nm. The methodology of the study will be presented in the next two sections. For a more complete description of the optical model the reader is referred to [11].

2. – Aerosol physical and optical properties

The atmospheric backscatter of lidar pulses is generated by the combined effect of molecular β_m and aerosols β_a backscatter cross-sections [12]. Typical 532 nm, mid-latitude values for β_m at 15, 18 and 25 km are of the order of 2.5×10^{-9}, 1.6×10^{-9}, and 5.3×10^{-10} cm^{-1} sr^{-1}, respectively [11]. While stratospheric background aerosols cross-sections at 532 nm hardly exceed $\beta_a = 10^{-10}$ cm^{-1} sr^{-1}, volcanic aerosols and STS PSC span the region 10^{-9}–10^{-8} cm^{-1} sr^{-1} and heavy volcanic and ice PSC can grow in excess of $\beta_a = 10^{-8}$ cm^{-1} sr^{-1}. Typical lidar-detectable aerosol backscatter is of the order of $\beta_a \approx 10^{-11}$ cm^{-1} sr^{-1} [11]. In lidar analysis, the scattering ratio $R = (\beta_a + \beta_m)/\beta_m$ is commonly employed to represent the aerosol contribution to the total backscatter, $R = 1$ indicating an aerosol-free atmosphere. At 532 nm, the 18 km background aerosol layer shows then typical values of $R \approx 1.06$. This is to be compared to maximum post-Pinatubo observations of $R \approx 100$ at 25 km in the tropics [13] and $R \approx 10$ at midlatitude [14]. In the case of PSC, STS attain scattering ratios of up to $R \approx$ 4-5, while ice ones can reach values of the order of $R \approx 100$ [15]. As for increasing wavelengths the molecular backscatter decreases much faster than the aerosol one, R at 694 nm is larger than at 532 nm. Typical values of R at 694 nm will be derived in the next sections.

At the wavelength λ, the backscatter efficiency $Q_{bs}(r, \lambda, m)$ and the extinction efficiency $Q_{ext}(r, \lambda, m)$ of homogeneous, spherical particles of radius r and complex refractive index $m = m_{re} - im_{im}$ can be computed by means of the Mie theory. The aerosol backscatter cross-section per unit air volume β_a, is then obtainable as

$$\beta_a = \int_0^\infty Q_{bs}(r, \lambda, m)\, n(r)\, \pi r^2\, dr\,, \tag{1}$$

where $n(r)$ is the particle size distribution. In a similar way, the extinction cross-section σ_a can be computed by replacing Q_{bs} by Q_{ext} in eq. (1). Knowledge of the aerosol extinction-to-backscatter ratio $R_{eb} = \sigma_a/\beta_a$ is fundamental to the correction for extinction in the inversion of lidar profiles and to the cross comparison of lidar and satellite extinction observations [11].

Many curves have been employed to fit the size distribution of stratospheric aerosols: gamma, lognormal, power law, etc. [16]. The lognormal, reported below, is often used because it well reproduces the bell-shaped dispersion (in log-log coordinates) of observed aerosol distributions [17]:

$$n(r) = \frac{dn}{dr} = \frac{N_0}{r\sqrt{2\pi}\ln\sigma_g}\exp\left[\frac{-\ln^2(r/r_g)}{2\ln^2(\sigma_g)}\right]. \tag{2}$$

In eq. (2), N_0 indicates the total number of particles per unit volume, r_g and σ_g the distribution geometric radius and width, respectively. Typical background aerosol distributions at 18-20 km are well fitted by a monomodal lognormal with parameters $N_0 = 10\ \mathrm{cm}^{-3}$, $r_g = 0.0725\,\mu\mathrm{m}$, and $\sigma_g = 1.86$ [18]. Volcanic injections perturb background conditions by generating large amounts of sulphuric acid which both condenses onto pre-existing aerosols and homogeneously nucleates fine, fast-coagulating particles. These processes often involve the buildup of bimodal distributions, characterized by a large-particle mode in the micron-size range. Bimodality is commonly observed after major volcanic eruptions [19-21, 17], and must be considered when evaluating aerosol optical properties [11].

3. – Aerosol scattering model

The aim of this paper is to provide relationships between β_a at 694 nm and aerosols parameters as total surface area S_a, volume V_a, extinction-to-backscatter ratio $R_{eb} = \sigma_a/\beta_a$, extinction σ_a, and effective radius r_{eff}. The latter parameter, defined as

$$r_{eff} = \frac{\int_0^\infty n(r)\, r\pi r^2\, dr}{\int_0^\infty n(r)\, \pi r^2\, dr} \tag{3}$$

was not considered in [11], but is often employed for characterizing a distribution typical size [9]. As proceeded in the 532 nm case [11], this aim is pursued via a statistical approach, *i.e.* evaluating such relationships by means of the Mie theory for a large number of aerosol size distributions, representative of conditions ranging from background to postvolcanic. Functional links between these variables are then found on the basis of the average values of the dispersion of computed relationships. As the number of observations of real size distributions is limited, the problem is approached using a Monte Carlo technique, *i.e.* generating random distributions and compositions whose parameters are constrained within experimentally observed boundaries. According to previous considerations, distributions are chosen to be monomodal and bimodal lognormals. Referring to the first and second mode by subscripts 1 and 2, respectively, six parameters (N_1, r_1, σ_1, N_2, r_2, and σ_2) plus real (m_{re}) and imaginary

TABLE I. – *Minimum and maximum values bounding the random variability of distribution parameters employed in simulations.*

Run	$N_1(\mathrm{cm}^{-3})$		$r_1(\mathrm{cm}^{-3})$		σ_1		$N_2(\mathrm{cm}^{-3})$	
694	1.0	30.0	$2.0\cdot10^{-6}$	$4.0\cdot10^{-5}$	1.3	2.3	$1.0\cdot10^{-4}$	4.0
532	1.0	30.0	$2.0\cdot10^{-6}$	$4.0\cdot10^{-5}$	1.3	2.3	$1.0\cdot10^{-4}$	4.0

Run	$r_2(\mathrm{cm}^{-3})$		σ_2		m_{re}		m_{im}	
694	$1.5\cdot10^{-5}$	$3.0\cdot10^{-4}$	1.1	1.8	1.410	1.450	−0.0	$-1.0\cdot10^{-6}$
532	$1.5\cdot10^{-5}$	$3.0\cdot10^{-4}$	1.1	1.8	1.420	1.460	−0.0	$-1.0\cdot10^{-6}$

(m_{im}) parts of the refractive index are randomly generated to compute each distribution optical properties. Selection of boundaries and acceptance rules for the generation of these parameters have been established on the basis of a large set of field observations reported in the literature and described in [11]. In this way, all possible distributions and compositions generated within the experimentally determined limits are statistically represented in the simulations. This work will address the "reference" aerosol case (run 99 in [11]), which was demonstrated to be the best model for background to heavy volcanic sulphate aerosols and also for liquid PSC with refractive index m_{re}, varying between 1.37 and 1.5 (run 96, in [11]). Conversely, this model is not representative of early volcanic conditions, when high supersaturation leads to the homogeneous nucleation of large numbers of new particles [11]. However, these transient conditions extend only to the first 1-2 months after the eruption, *i.e.* until coagulation brings down the total number of particles to typical stratospheric values [3, 22]. For comparison purposes, the 532 nm simulation will be run again and presented. At both the 694 and 532 nm wavelengths, a new variability range of the refractive index as obtained from recent results reported by Russell *et al.* [9] will be employed. All boundaries to the variability of distribution parameters are summarized in table I. Different runs are numbered according to the relevant wavelength. Ten thousand distributions (2 000 more than in [11]) are considered in each simulation. For every distribution, β_{a} and σ_{a}, S_{a}, V_{a} and r_{eff} are integrated over the radius range 0.001 to 25 μm. Convergence of the integral is accepted when resulting better than 1/50 000.

4. – Model results

4˙1. *Aerosol surface area.* – Average values and relative errors for the relationships S_{a} *vs.* β_{a} at the two wavelengths are presented in figs. 1a and 1b, respectively. In this and the following cases, average values are computed at eight, equally spaced bins per decade. To be considered in the analysis, such bins must include at least 100 distributions. Every average point is represented by one plotted symbol. Throughout the discussion, model errors will be referred to as the 1σ dispersion of the investigated parameter (presently the aerosol surface area S_{a}) resulting from each simulation. Errors in the lidar evaluation of the independent variable β_{a} are expected to be much smaller than the model ones (order of 2% as soon as aerosol grow). Since these errors also depend on system characteristics, they will not be considered in the model error analysis.

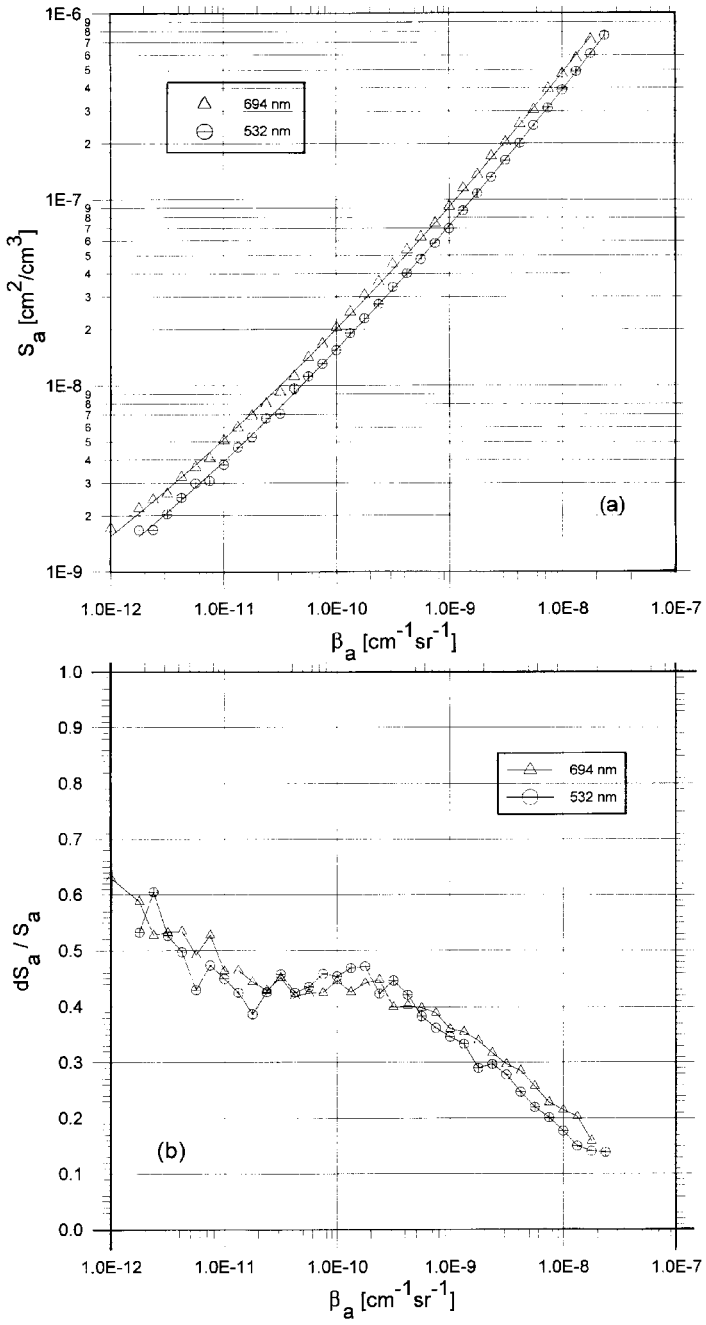

Fig. 1. – (a): Average value points of the relationships S_a *vs.* β_a computed at 694 (open triangles) and 532 nm (crossed circles). Solid lines show the log-log, second-order polynomial fit to the relevant points. Fit parameters are reported in table II. (b): Relative errors dS_a/S_a ($dS_a = 1\sigma$) of fit estimates presented in (a).

Backscatter cross-sections β_a obtained in run 694 range between 1×10^{-12} and 2×10^{-8} cm^{-1} sr^{-1}, spanning 4 orders of magnitude. At 532 nm, β_a values range between 2×10^{-12} and 3×10^{-8} cm^{-1} sr^{-1}. The largest cross-section aerosols achieved within these boundaries can therefore account for a 532 nm scattering ratio $R \geqslant 10$ upward of 15 km altitude and $R \approx 40$ at 25 km. At 694 nm, due to the λ^{-4}-dependence of molecular scattering, and to the approximate λ^{-1}-dependence of the aerosol backscatter, this converts to scattering ratios $R \geqslant 20$ upward of 15 km and to $R \approx 80$ at 25 km. The relevant range for S_a is $1.5 \times 10^{-9} \div 8 \times 10^{-7}$ cm^2 cm^{-3} (0.15–80 μm^2 cm^{-3}), spanning almost 3 orders of magnitude. As found in [11], logarithmic-coordinates relationships S_a, V_a, and R_{eb} *vs.* β_a are well approximated by a second-order polynomial (parabolic) curve of the kind

$$Y = a_{0Y} + a_{1Y} X + a_{2Y} X^2 , \tag{4}$$

where $X = \log \beta_a$ and Y is the logarithm of the parameter investigated, in this case S_a. The corresponding equation to evaluate S_a is then

$$S_a = 10^{(a_{0S} + a_{1S} X + a_{2S} X^2)} . \tag{5}$$

Least-squares parabolic fits to the runs average values and their relevant parameters a_{0S}, a_{1S}, and a_{2S} are reported in fig. 1a as solid lines and in table II, respectively. The range of backscatter cross-sections over which the fit is computed and the correlation coefficient, representing the quality of the parabolic approximation, are also reported in table II. Dispersion of results about their average value provides a further characterization of simulations. Figure 1b reports such relative errors dS_a/S_a ($dS_a = 1\sigma$ dispersion of computed surface area values) *vs.* β_a, for the two cases presented in fig. 1a. These plots are representative of the accuracy of the model at estimating S_a. While in the region of background aerosols ($7 \times 10^{-12} \leqslant \beta_a \leqslant 10^{-10}$ cm^{-1} sr^{-1} at 694 nm) all relative errors range between 40 and 50%, dS_a/S_a descends below 40% for volcanic/STS PSC conditions ($\beta_a \approx 10^{-9}$ cm^{-1} sr^{-1}) and values of 10–15% in the heavy

TABLE II. – *Coefficients of logarithmic parabolic fits* (*eq.* (4)) *to model-derived average values of the variables* (Var): *surface area* S_a(cm^2/cm^3), *volume* V_a(cm^3/cm^3), *extinction* σ_a(cm^{-1}), *extinction-to-backscatter ratio* $R_{eb} = \sigma_a/\beta_a$(sr) *and effective radius* r_{eff}(cm) *as a function of backscatter cross-section* β_a(cm^{-1} sr^{-1}) *at* 694 *and* 532 nm. β_{min} *and* β_{max}(cm^{-1} sr^{-1}) *define the region over which the fit was computed. The parabolic regression correlation coefficients r indicate quality of the fit.*

Run	Var	β_{min}	β_{max}	a_0	a_1	a_2	r
694	S_a	$0.10 \cdot 10^{-11}$	$0.18 \cdot 10^{-07}$	1.8665	1.2892	0.0333	0.9997
532	S_a	$0.17 \cdot 10^{-11}$	$0.23 \cdot 10^{-07}$	1.8671	1.3027	0.0335	0.9998
694	V_a	$0.10 \cdot 10^{-11}$	$0.18 \cdot 10^{-07}$	− 0.2304	1.6024	0.0342	0.9999
532	V_a	$0.17 \cdot 10^{-11}$	$0.23 \cdot 10^{-07}$	− 0.1023	1.6415	0.0352	0.9999
694	σ_a	$0.10 \cdot 10^{-11}$	$0.18 \cdot 10^{-07}$	− 3.8894	− 0.1393	− 0.0576	0.9999
532	σ_a	$0.17 \cdot 10^{-11}$	$0.23 \cdot 10^{-07}$	− 4.8636	− 0.3123	− 0.0655	1.0000
694	σ_a/β_a	$0.10 \cdot 10^{-11}$	$0.18 \cdot 10^{-07}$	− 3.8809	− 1.1386	− 0.0577	0.9717
532	σ_a/β_a	$0.17 \cdot 10^{-11}$	$0.23 \cdot 10^{-07}$	− 4.9027	− 1.3221	− 0.0661	0.9940
694	r_{eff}	$0.10 \cdot 10^{-11}$	$0.18 \cdot 10^{-07}$	− 2.1843	0.1954	− 0.0045	0.9994
532	r_{eff}	$0.17 \cdot 10^{-11}$	$0.23 \cdot 10^{-07}$	− 2.0104	0.2345	− 0.0028	0.9990

volcanic/ice PSC conditions ($\beta_a \approx 10^{-8}$ cm^{-1} sr^{-1}). Both Ruby-lidar and 532 nm surface estimates are then affected by smaller errors in the presence of larger aerosols. This behaviour differs from the one of particle counters, whose errors increase with the lowering in the number concentrations, *i.e.* for larger particles [23]. In this respect, when evaluating Pinatubo aerosols surface area, Deshler *et al.* [17] reported optical counter average errors to range between 10 and 20%, with maxima of 60%. Therefore, expected errors of S_a estimates at both 694 and 532 nm wavelengths well compare with the ones characterizing *in situ*, particle counter observations.

4˙2. *Aerosol volume.* – Average points of the relationships V_a *vs.* β_a and relevant errors dV_a/V_a *vs.* β_a are plotted in figs. 2a and 2b, respectively. All points in fig. 2a are well approximated by the second-order polynomial fits of eq. (4), plotted as a solid line. Fit parameters and boundaries are reported in table II. Similarly to backscatter cross-sections, particles volume spans 4 orders of magnitude. This is the largest dynamical range amongst all the parameters investigated. For background aerosols, the 694 nm curve shows the typical sulphates volume $V_a < 0.1\ \mu$m^3 cm^{-3}, which grows to $V_a > 1\ \mu$m^3 cm^{-3} in volcanic/PSC conditions.

Errors of volume estimates (fig. 2b) follow patterns opposite to the surface area ones. In the region of background aerosols, errors of less than 20% point at volume estimates as more accurate than surface area ones. However, dV_a/V_a values increase (to approximately 25% at 694 nm) in heavy volcanic/ice PSC conditions. Overall, Ruby-lidar volume estimates are affected by errors slightly lower than at 532 nm. At both wavelengths errors remain comparable to those reported for *in situ* particle counters (10-20% on average [17]).

4˙3. *Extinction-to-backscatter ratio.* – Average value points of the extinction-to-backscatter ratio, $R_{eb} = \sigma_a/\beta_a$ and relevant errors dR_{eb}/R_{eb} as a function of β_a are plotted in figs. 3a and 3b, respectively. In fig. 3a the parabolic fits to R_{eb} are also plotted as solid lines. The relevant coefficients are provided as variable σ_a/β_a in table II. Up to approximately $\beta_a = 3 \times 10^{-11}$ cm^{-1} sr^{-1}, values of R_{eb} are pretty similar at both wavelengths. Beyond that point the two curves separate, the ratio being smaller the shorter the wavelength. Maxima of approximately $R_{eb} = 56$ and $R_{eb} = 51$ sr are reached at 694 and 532 nm, respectively. The two curves tend to converge again in the large cross-sections limit. In the case of volcanic aerosols or PSC ($\beta_a \geqslant 10^{-9}$ cm^{-1} sr^{-1}), both plots show R_{eb} to decrease for increasing β_a, in good agreement with the behavior of R_{eb} at 532 nm as reported by Jager and Hofmann [21] and with the vertically resolved, R_{eb} profiles of the Pinatubo cloud obtained by Ansmann *et al.* [24] at 308 nm. In typical volcanic conditions, R_{eb} at 694 and 532 nm do not differ by more than 10%. However, when passing from background to heavy volcanic conditions, R_{eb} undergoes a change larger than 50%. Such behavior demonstrates the importance of employing suitable R_{eb} values when inverting and comparing lidar observations taken in different conditions and at different wavelengths. Correlation coefficients reported in table II show that, being a composed parameter, the quality of parabolic fits to the R_{eb} *vs.* β_a relationship is somewhat poorer than for the other parameters. However, relative errors of R_{eb} estimates at 694 nm (fig. 3b) are generally lower than 35%, and reach a minimum of 20–25% in the regions of background and heavy volcanic/ice PSC particles. Error patterns are pretty similar at both 694 and 532 nm wavelengths. Altogether, model accuracy is consistent with the values (15–50%) characterizing determination of R_{eb} by means of Raman lidar [24].

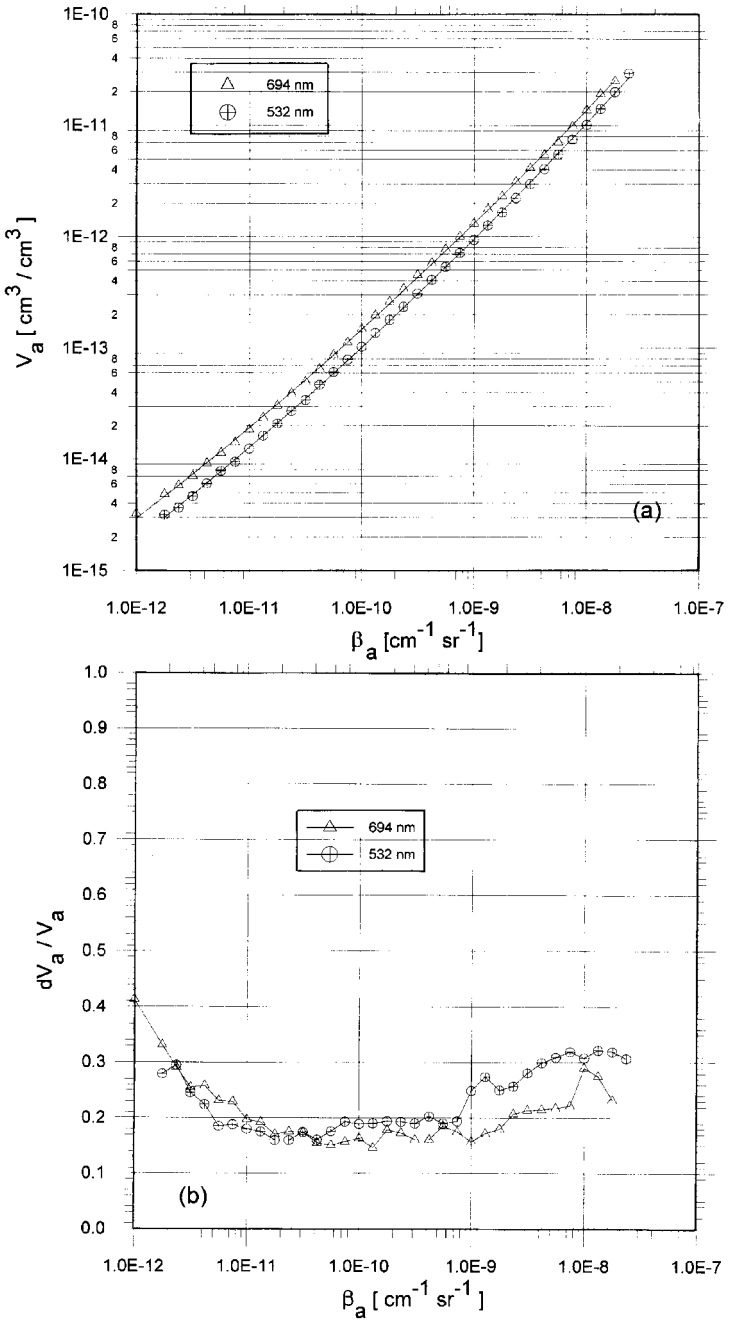

Fig. 2. – (a): Average value points of the relationships V_a *vs.* β_a computed at 694 and 532 nm. Solid lines show the log-log, second-order polynomial fit to the relevant points. Fit parameters are reported in table II. (b): Relative errors dV_a/V_a ($dV_a = 1\sigma$) of fit estimates presented in (a).

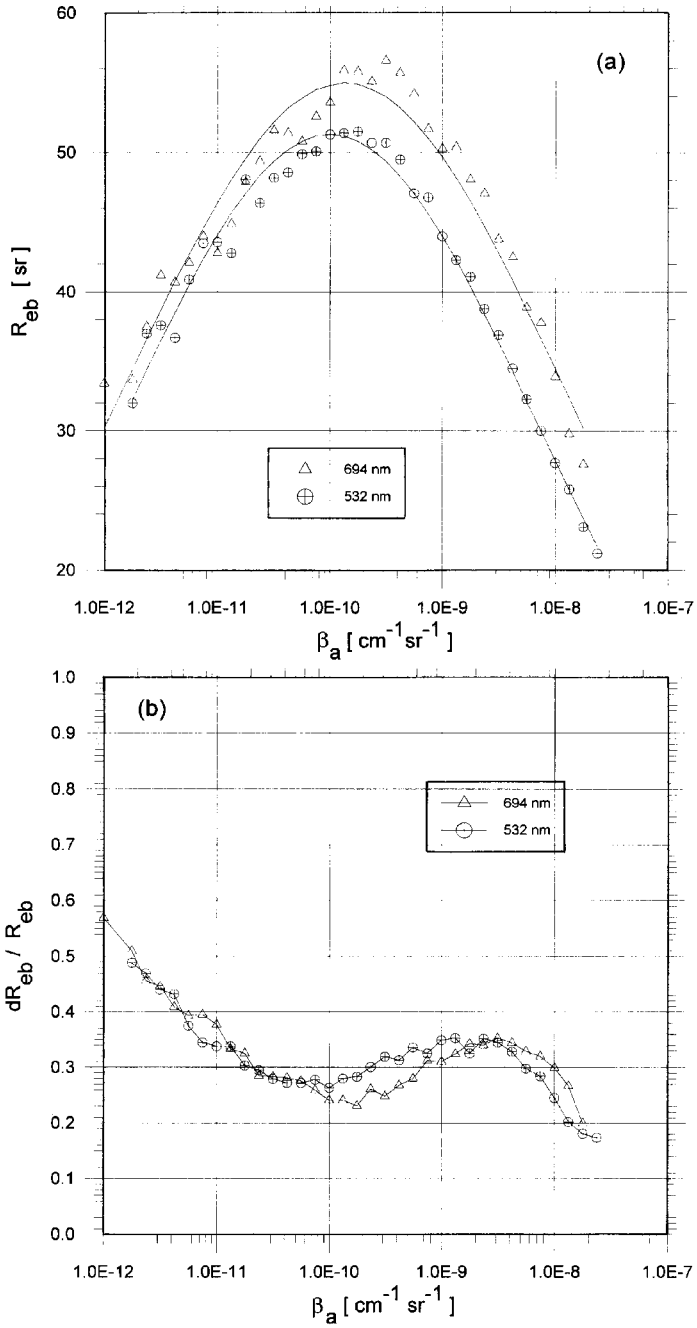

Fig. 3. – (a): Average value points of the relationships R_{eb} *vs.* β_a computed at 694 and 532 nm. Solid lines show the log-log, second-order polynomial fit to the relevant points. Fit parameters are reported in table II. (b): Relative errors dR_{eb}/R_{eb} ($dR_{eb} = 1\sigma$) of fit estimates presented in (a).

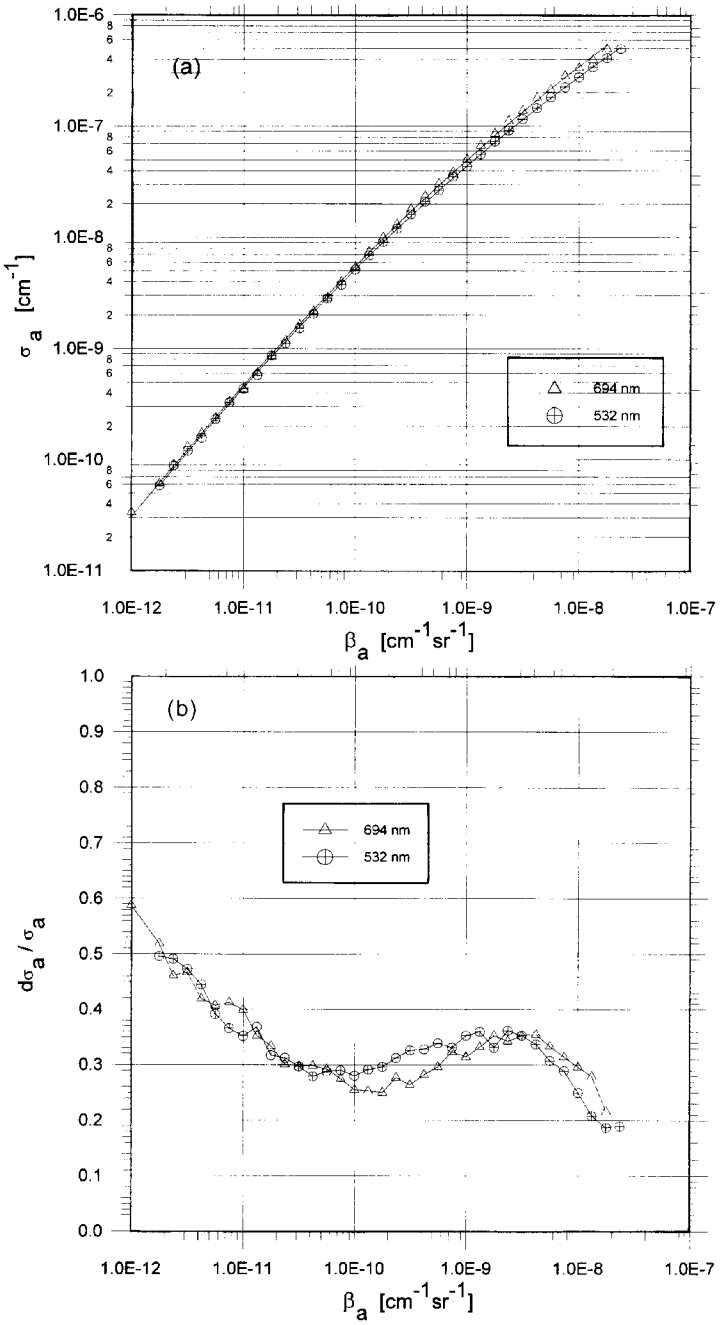

Fig. 4. – (a): Average value points of the relationships σ_a *vs.* β_a computed at 694 and 532 nm. Solid lines show the log-log, second-order polynomial fit to the relevant points. Fit parameters are reported in table II. (b): Relative errors $d\sigma_a/\sigma_a$ ($d\sigma_a = 1\sigma$) of fit estimates presented in (a).

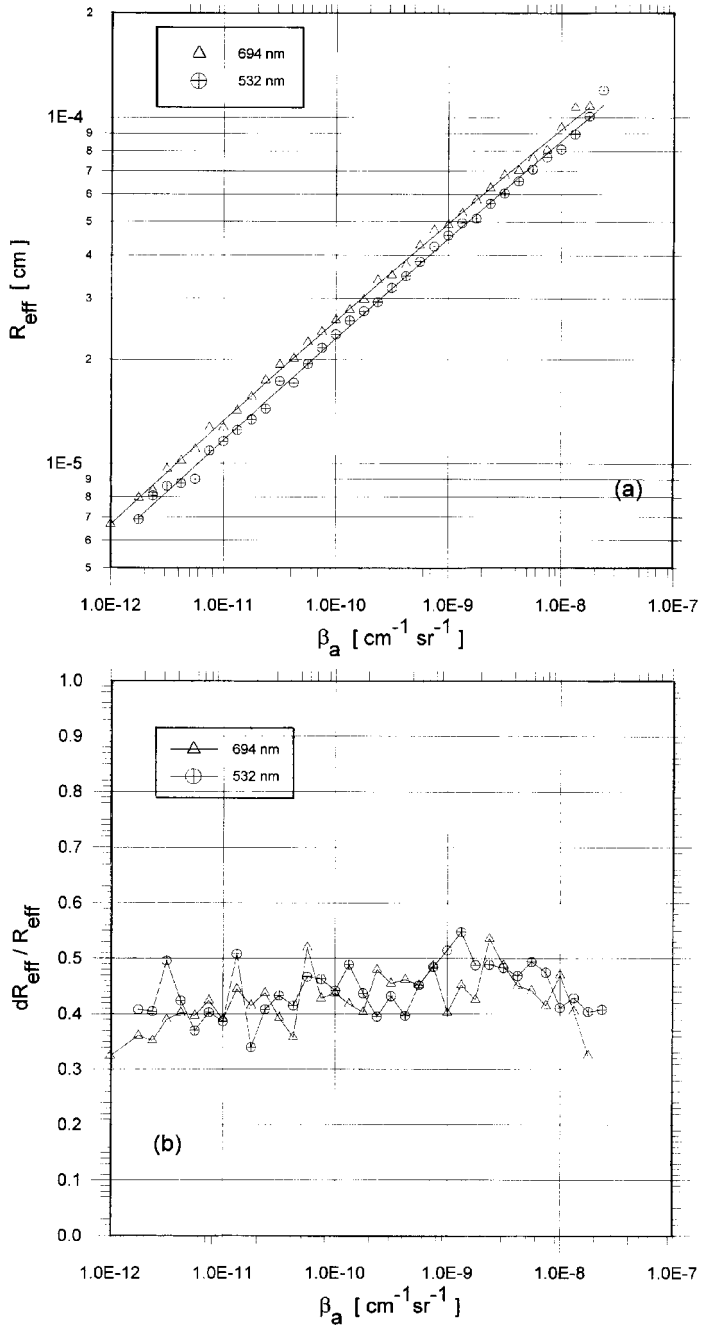

Fig. 5. – (a): Average value points of the relationships r_{eff} *vs.* β_a computed at 694 and 532 nm. Solid lines show the log-log, second-order polynomial fit to the relevant points. Fit parameters are reported in table II. (b): Relative errors $dr_{\text{eff}}/r_{\text{eff}}$ ($dr_{\text{eff}} = 1\sigma$) of fit estimates presented in (a).

Together with the lidar relevant R_{eb} ratio, it is useful to present the direct relationship between extinction and backscatter cross-sections obtained by the model. In fact, such link allows direct comparison between lidar and extinction observations. Average points of the σ_a *vs.* β_a relationship and relevant errors are plotted in figs. 4a and 4b, respectively. In table II are reported as variable σ_a the coefficients a_{xE} of the second-order polynomial fits to the extinction *vs.* backscatter relationships drawn as solid lines in fig. 4a. These plots show that at both wavelengths the link between σ_a and β_a is be quite similar in the region of background aerosol, while some differences appear when particles grow larger. These results show that direct inference of aerosol extinction from lidar observations is characterized by an error oscillating between 20 and 35% all over the range of observable particles (fig. 4b).

4·4. *Effective radius.* – Points of average relationships between the distribution effective radius r_{eff} and β_a are plotted in fig. 5a. Relevant errors dr_{eff}/r_{eff} are shown in fig. 5b. When switching from background to volcanic/PSC conditions, r_{eff} increases approximately from 0.15 to 0.6 μm. Such behavior is in good agreement with observations reported by several authors after the Mt. Pinatubo eruption [9]. The second-order polynomial fits (solid lines in fig. 5a) follow a quasi-linear behaviour. Relevant parameters are presented in table II. In most aerosol conditions, relative errors shown in fig. 5b range between 40 and 50%, indicating the effective radius as the distribution parameter suffering the highest variability. However, Russell *et al.* [9] show that inference of r_{eff} by means of various remote-sensing techniques is characterized by errors ranging between 20 and 100%, *i.e.* even larger than the present-model ones. Errors of *in situ* observations are not presented in [9]. In general, larger estimate errors and small dynamical range between background and volcanic/PSC conditions make the distribution effective radius a variable less favourable than the previous ones for characterizing stratospheric aerosols on the basis of lidar observations.

5. – Conclusions

Functional relationships for estimating stratospheric aerosol surface area, volume, extinction-to-backscatter ratio, extinction, and effective radius from single-wavelength, 694 nm Ruby-lidar measurements have been determined. These relationships have been obtained computing Mie scattering properties (β_a, σ_a) of sets of 10 000 aerosol distributions and compositions, whose parameters were randomly generated according to boundary conditions derived from experimentally observed size distributions. These simulated aerosols are representative of worldwide stratospheric conditions including from background to postvolcanic sulphate particles and liquid polar stratospheric clouds (STS). Analytic expressions describing such properties have been derived from least-squares fitting of the average relationships linking the investigated parameters and aerosol backscatter. In log-log coordinates, these average points are well fitted by a second-order polynomial curve. Results have been compared to the ones obtained at 532 nm by the original optical model [11]. Functional relationships and relevant errors were found to follow similar patterns at both wavelengths.

Relative errors of the optical model at 694 nm range between 15 and 45% for surface area, being smaller at larger cross-sections. In the case of volume estimates, errors are of the order of 20%, slightly increasing in heavy volcanic conditions. Errors

characterizing extinction-to-backscatter ratio and extinction estimates oscillate in the 20–35% range, and minimize in heavy volcanic/PSC conditions. At all wavelengths, these errors are comparable to the ones characterizing measurements obtained by operational, *in situ* techniques. Effective radius estimates suffer from a small dynamical range of the parameter and relative errors of 40–55%. These conditions make r_{eff} a less favourable output of the model, characterized by errors of magnitude similar to the one of indirect techniques. As surface area errors strongly decrease at larger backscatter cross-sections, *i.e.* in the presence of volcanic clouds and PSC, application of the model to Ruby-lidar observations provides a good tool for estimating a parameter so important in ozone-depletion studies. In the case of aerosol volume, the 694 nm model allows a slightly better evaluation than the 532 nm one, confirming, however, the good capability of the method at estimating aerosol volume and mass. Inference of a composite parameter as the extinction-to-backscatter ratio is characterized by a slightly lower quality of the fits. However, as R_{eb} halves in passing from moderate to heavy volcanic/PSC conditions, use of the analytic relationships provided by the model allows more realistic assumptions than the one of constant ratio, often employed in these cases. As a general rule, model relative errors and fit quality indicate the Ruby laser as very well suited for estimating stratospheric aerosol physical properties by means of single-wavelength lidar observations.

* * *

This work was partly supported by the Italian Space Agency, ASI.

REFERENCES

[1] HANSEN J., SATO M., LACIS A. and RUEDY R., *The missing climate forcing, Philos. Trans. R. Soc. London, B*, **352** (1997) 231-240.

[2] WORLD METEOROLOGICAL ORGANIZATION (WMO), *Scientific Assessment of Ozone Depletion: 1994*, Report 37, Geneva, 1995.

[3] MICHELANGELI D. V., ALLEN M., and YUNG Y. L., *El Chichon volcanic aerosols: Impact of radiative, thermal, and chemical perturbations, J. Geophys. Res.*, **94** (1989) 18429-18443.

[4] TURCO R. P., WHITTEN R. C. and TOON O. B., *Stratospheric aerosols: Observation and theory, Rev. Geophys.*, **20** (1982) 233-279.

[5] MIDDLEBROOK A. M., IRACI L. T., MCNEILL L. S., KOEHLER B. G., SAASTAD O. W., TOLBERT M. A. and HANSON D. R., *FTIR studies of thin film* H_2SO_4/H_2O *films: Formation, water uptake, and solid-liquid phase changes, J. Geophys. Res.*, **98** (1993) 20473-20481.

[6] KOOP T. and CARSLAW K. S., *Melting of* H_2SO_4-$4H_2O$ *particles upon cooling: Implications for polar stratospheric clouds, Science*, **272** (1996) 1638-1641.

[7] STEELE H. M. and HAMILL P., *Effects of temperature and humidity on the growth and optical properties of sulfuric acid-water droplets in the stratosphere, J. Aerosol Sci.*, **12** (1981) 517-528.

[8] YUE G. K., POOLE L. R., WANG P. H. and CHIOU E. W., *Stratospheric aerosol acidity, density and refractive index deduced from SAGE II and NMC temperature data, J. Geophys. Res.*, **99** (1994) 3727-3738.

[9] RUSSELL P. B., LIVINGSTON J. M., PUESCHEL R. F., BAUMAN J. J., POLLACK J. B., BROOKS S. L., HAMILL P., THOMASON L. W., STOWE L. L., DESHLER T., DUTTON E. G. and BERGSTROM R. W., *Global to microscale evolution of the Pinatubo volcanic aerosol derived from diverse measurements and analyses, J. Geophys. Res.*, **101** (1996) 18745-18763.

[10] MOLINA M. J., ZHANG R., WOOLDRIDGE P. J., MCMAHON J. R., KIM J. E., CHANG H. Y. and BEYER K. D., *Physical chemistry of the* $H_2SO_4/HNO_3/H_2O$ *system: Implications for polar stratospheric clouds*, *Science*, **261** (1993) 1418-1423.

[11] GOBBI G. P., *Lidar estimation of stratospheric aerosol properties: Surface, volume and extinction to backscatter ratio*, *J. Geophys. Res.*, **100** (1995) 11219-11235.

[12] COLLIS R. T. H. and RUSSELL P. B., *Lidar measurement of particle and gases by elastic backscattering and differential absorption*, in *Laser Monitoring of the Atmosphere*, edited by E. D. HINKLEY (Springer-Verlag, New York), 1976 pp. 71-145.

[13] WINKER D. M. and OSBORN M. T., *Airborne lidar observations of the Pinatubo volcanic plume*, *Geophys. Res. Lett.*, **19** (1992) 167-170.

[14] GOBBI G. P., CONGEDUTI F. and ADRIANI A., *Early stratospheric effects of the Pinatubo eruption*, *Geophys. Res. Lett.*, **19** (1992) 997-1000.

[15] GOBBI G. P., DI DONFRANCESCO G. and ADRIANI A., *Physical properties of stratospheric clouds during the Antarctic winter of 1995*, *J. Geophys. Res.*, **103** (1998) 10859-10873.

[16] RUSSELL P. B., SWISSLER T. J., MCCORMICK M. P., CHU W. P., LIVINGSTON J. M. and PEPIN T. J., *Satellite and correlative measurements of the stratospheric aerosol, I, An optical model for data conversion*, *J. Atmos. Sci.*, **38** (1981) 1279-1294.

[17] DESHLER T., JOHNSON B. J. and ROZIER W. R., *Balloonborne measurements of Pinatubo aerosol during 1991 and 1992 at 41N: Vertical profiles, size distribution, and volatility*, *Geophys. Res. Lett.*, **20** (1993) 1435-1438.

[18] PINNICK R. G., ROSEN J. M. and HOFMANN D. J., *Stratospheric aerosol measurements, III, Optical model calculations*, *J. Atmos. Sci.*, **33** (1976) 304-313.

[19] HOFMANN D. J. and ROSEN J. M., *Stratospheric sulfuric acid fraction and mass estimate for the 1982 volcanic eruption of El Chichon*, *Geophys. Res. Lett.*, **10** (1983) 313-316.

[20] SNETSINGER K. G., FERRY G. V., RUSSELL P. B., PUESCHEL R. F. and OBERBECK V. R., *Effects of the El Chichon on stratospheric aerosols, late 1982 to early 1984*, *J. Geophys. Res.*, **92** (1987) 761-771.

[21] JAGER H. and HOFMANN D. J., *Midlatitude lidar backscatter to mass, area, and extinction conversion model based on in situ aerosol measurements from 1980 to 1987*, *Appl. Opt.*, **30** (1991) 127-138.

[22] TURCO R. P. and YU F., *Aerosol invariance in expanding coagulating plumes*, *Geophys. Res. Lett.*, **24** (1997) 1223-1226.

[23] HOFMANN D. J., ROSEN J. M., HARDER J. W. and HEREFORD J. V., *Balloon-borne measurements of aerosol, condensation nuclei, and cloud particles in the stratosphere at McMurdo Station, Antarctica, during the spring of 1987*, *J. Geophys. Res.*, **94** (1989) 11253-11269.

[24] ANSMANN A., WANDINGER U. and WEITKAMP C., *One-year observations of Mount-Pinatubo aerosol with an advanced raman lidar over Germany at 53.5N*, *Geophys. Res. Lett.*, **20** (1993) 711-714.